# Photocatalytic degradation of efavirenz and nevirapine using visible light-activated Ag-AgBr-LDH nanocomposite catalyst

Lehlogonolo Tabana [*], Davy-Rayn Booysens, Shepherd Tichapondwa

*Department of Chemical Engineering, Sustainable Environmental and Water Utilisation Processes Division, University of Pretoria, Pretoria 0028, South Africa*

## ARTICLE INFO

## ABSTRACT

Antiretroviral drugs (ARVDs) are one of the many classes of emerging pharmaceutical pollutants that have been detected in South African waterbodies in recent years. Efavirenz (EFV) and nevirapine (NVP) are commonly used drugs in antiretroviral therapy (ART) in the region and have been reported to be persistent in wastewater. Their presence in water poses health hazards to human beings and the aquatic environment. It is therefore important that these compounds be remediated from the environment. Visible light activated photocatalysis is one of the sustainable remediation technologies that aptly removes refractory organic contaminants from various water matrices. This study reports for the first time, the synthesis of silver halide doped Mg-Zn-Al LDH clay as a photocatalyst in the degradation of selected ARVDs under visible light irradiation. The physicochemical properties of the photocatalyst were elucidated using a range of characterization techniques. Response surface modelling was used to evaluate the interactions between the independent variables: initial pH of the solution, photocatalyst loading and initial concentration of the pollutants. The results showed that there were significant interactions between initial concentration and photocatalyst loading for EFV degradation while the interactions between photocatalyst loading and initial concentration, and initial pH of the solution and photocatalyst loading were significant for NVP degradation. The highest degradation efficiencies were 84 and 100% for EFV and NVP, respectively. Scavenger tests revealed that the hydroxyl free radicals and photo-induced holes were the dominant active species that promoted the degradation of ARVDs. The synthesized photocatalyst nanocomposite demonstrated its efficacy in degradation of ARVDs in water under visible light irradiation.

## 1. Introduction

Human immunodeficiency virus (HIV) and acquired immune deficiency syndrome (AIDS) have been a major public health issue in Africa for over four decades. According to the Joint United Nations Programme on HIV/AIDS (UNAIDS), Sub-Saharan Africa was the most affected region in 2020, with an estimated 25.7 million people living with HIV and AIDS. Since the outbreak of the pandemic in the early 1980 s, it is estimated that over 15 million AIDS related deaths have occurred in this region by the year 2020. The Southern African region is of particular concern since it is reported to have the continent's highest HIV prevalence rates. South Africa, Botswana, Eswatini, Namibia, Zambia, and Zimbabwe report prevalence rates ranging from 15% to 36% of the population [1]. Due to the severity of the disease, numerous ARVDs have been developed to reduce the viral load in infected individuals and prevent mother-to-child transmissions. ARVDs prevent the virus from replicating in the body, decreasing the amount of virus in the

bloodstream, and slowing the progression of the disease [2]. Due to the inability of ARVDs to completely eradicate the virus, infected patients must take this medication for the rest of their lives. Recent estimates by Schoeman *et. al.* [3] indicate that a single patient requires approximately 990 mg per day of ARVD combination therapy which includes EFV and NVP. Since the rate of ARVD consumption, based on epidemiological statistics of various African countries, is relatively uncertain, it is difficult to precisely estimate the quantity of ARVDs consumed on the continent over time [4]. To put this into perspective, recent estimates in South Africa indicate that 7 million individuals may be HIV-positive. According to a report by the World Health Organization, more than 70% of AIDS patients were receiving antiretroviral therapy; this suggests that the daily consumption of ARVDs is approximately 5.2 tons, or 1,898 tons annually. The excretion of ARVDs and their associated metabolites differs between compounds. Significant proportions of EFV and NVP are metabolized in the liver and eliminated via the kidneys, while small amounts are eliminated via urine and faeces [5]. EFV and NVP are

* Corresponding author.
    *E-mail address:* tabana.ls@tuks.co.za (L. Tabana).

excreted unchanged in urine at rates of 14 and 5%, respectively, in single doses [6,7]. Assuming a typical excretion rate of 30% of ingested ARVDs reports to sewage via urine and faeces, it is estimated that 569 tons of drugs could reach South Africa's aquatic systems annually.

The increased detection of ARVDs and other pharmaceuticals in aquatic systems has led to their classification as emerging compounds. EFV and NVP were discovered to be among the ARVDs that are persistent in waterbodies [1,8,9]. Studies by multiple researchers have reported influent wastewater treatment plant (WWTP) concentrations of up to 34,000 ng/L and effluent concentrations as high as 33,000 ng/L. These values indicate that conventional WWTPs that typically rely on technologies such as activated sludge treatment, are ineffective in removing ARVDs. Even at low concentrations, ecotoxicological and human assessment studies have revealed the potential long-term toxicity of these compounds. The dangers posed by ARVDs to non-target species have prompted the monitoring and remediation of their presence in waterbodies [8,10,11], particularly in nations with a substantial population on ART. Advanced oxidation processes (AOPs) are favored for the removal of recalcitrant pollutants in wastewater due to their low cost and rapid, nonselective oxidation rates and potential to completely mineralize organic pollutants. Although several AOPs exist, heterogeneous photocatalysis is regarded as one of the most viable processes due to its capacity to achieve greater degradation efficiencies, eco-friendliness, and ease of operation.

Layered double hydroxides (LDHs) clays are some of the materials that have attracted attention as photocatalysts for degradation of various organic pollutants [12]. This is due to their attractive physicochemical properties that include flexible compositions and structures, and higher specific areas [13]. Ternary LDH clays have been reported to perform better than binary LDH clays when applied in water remediation processes. This is due to the additional metal constituent which enhances the physical and chemical features of the material and ultimately the efficacy of the clay. Valente *et. al.* [14] reported that a Mg-Zn-Al LDH clay was 10 times more effective than Mg-Al LDH clay in degrading phenol and 2,4-dichlorophenoxyacetic acid under UV light irradiation. They attributed this to the presence of photoactive Zn metal in the clay composition. The amount of Zn in the LDH clay was controlled at a molar concentration of 5% as it presented a higher specific area than clays with elevated Zn content. A separate study by. Kim *et. al.* [15] revealed that addition of cobalt to a Zn-Al LDH clay doubled the performance of the clay in degrading methyl orange from wastewater.

Although extensive research has been conducted on the photocatalytic properties of LDH clays, their effectiveness is usually confined to the ultraviolet (UV) region of the electromagnetic spectrum, which comprises only a small portion (4 – 5%) of the solar spectrum [16]. This limitation is due to their large bandgap energy, which inhibits their ability to absorb visible light, which has a lower energy than UV light. Sherryna and Tahir [17] and Ng *et. al.* [18] reported that LDH clays possess bandgap energies ranging from 4 to 5 eV. This property restricts their light absorption capabilities to shorter wavelengths than 300 nm, that is in the UV region. As a result, their efficiency as photocatalysts for visible light-induced reactions is compromised, as they are unable to absorb visible light with wavelengths between 400 and 700 nm. Numerous studies have been conducted to improve the photocatalytic activity of LDHs under visible light irradiation, including doping them with transition metal ions [14,15] and modifying the interlayer anions of LDHs to alter their electronic structure and bandgap energy [19]. In addition, LDHs can be paired with materials that possess narrower bandgaps, such as carbon nitride [20,21], to create hybrid materials that can efficiently absorb visible light and facilitate photocatalytic reactions [22]. Another approach involves doping LDHs with materials that are effective in absorbing visible light, such as silver halides, to enhance their photocatalytic activity under visible light irradiation [23].

Silver halides (AgX, where X represents Cl, Br, or I) are some of the preferred dopant materials coupled to LDH clays for photocatalytic

applications due to their sensitivity to visible light [24]. However, these halides have limitations such as susceptibility to high rates of electron-hole pair recombination and photo-corrosion resulting in $Ag^0$ deposition surface of the photocatalyst which in turn renders the material unstable and less effective. Weng *et. al.* [25] and Huang *et. al.* [26] reported that these shortfalls can be made less significant by coupling Ag-AgX with robust materials. This would allow the metallic silver nanoparticles to undergo a surface plasmon resonance (SPR) phenomenon which enables them to effectively absorb visible light photons. These factors suggest that an Ag-AgX composite containing LDH clays will be stable and have increased photocatalytic activity. The primary objective of this study was to synthesize a nanocomposite photocatalyst, Ag-AgBr-LDH, with the capability of degrading ARVDs in water under visible light irradiation. To achieve this, the LDH clay was synthesized and modified to enhance its photocatalytic properties. Batch photodegradation experiments were conducted to evaluate the performance of the synthesized photocatalyst, while considering various operating parameters such as photocatalyst loading, initial pH of the solution, and the effect of pollutant concentration. Furthermore, a detailed investigation into the degradation mechanism of ARVDs was carried out to gain insights into the underlying processes involved in the photocatalytic degradation. The photostability and reusability of the photocatalyst were also assessed to determine its durability and performance upon repeated applications.

## 2. Experimental

### 2.1. Materials

Precursor chloride salts, aluminium chloride hexahydrate ($AlCl_3 \cdot 6H_2O$), magnesium chloride hexahydrate ($MgCl_2 \cdot 6H_2O$), and zinc chloride ($ZnCl_2$) were obtained from Glassworld in South Africa. Sodium hydroxide (NaOH), sodium bromide (NaBr), and silver nitrate ($AgNO_3$) were purchased as solid compounds from Merck (Pty) Ltd. The ARVDs, efavirenz and nevirapine, were sourced as solid powders from Adcock Ingram. Solvents used in the experiments were methanol (99%) and acetonitrile (99.9%), which were supplied as solutions by Sigma Aldrich. Hydrochloric acid (HCl) (32%) was also supplied as a solution by Sigma Aldrich, while acetic acid (99%) was obtained as a liquid from Glassworld. All the materials were utilized as received without further processing except for NaOH and HCl that were diluted prior to usage in pH adjustment. Deionised water dispensed by an Elga Purelab Flex 3 water purifier was used for all the experiments. A 72 W LED lamp with a peak wavelength range of 380 – 800 nm was used as a source of visible light irradiation.

### 2.2. Composite catalyst synthesis

#### 2.2.1. Synthesis of layered double hydroxide clay

LDH clay was synthesized using co-precipitation at a constant pH of 10 (± 0.25) to prevent the formation of metal hydroxides [26]. The co-precipitation synthesis method was selected because it provides a convenient and versatile approach for the preparation of LDH clays with controlled composition, uniform structure, high purity, and scalability [27] The required amounts of metal salts were dissolved in deionized water to create a 1 M solution based on cations with molar ratios of 75%, 5%, and 20% for Mg, Zn, and Al, respectively; a total volume of 250 mL was produced. The composition of LDH clay was carefully selected to optimize its physicochemical properties [28]. The salt solutions were added gradually to a 60 °C pre-heated 1 L glass reactor containing 250 mL of 1 M $Na_2CO_3$ solution. The pH of the slurry was maintained at 10 by adding the required amounts of 2 M NaOH solution. The resulting slurry was stirred at 500 rpm for 24 h. A Daihan Scientific magnetic stirrer (MSH-20D) with a hot plate and temperature controller was used to mix and regulate the temperature of the reactor's contents. After the reaction was complete, the suspensions were allowed to cool to room

temperature before being centrifuged at 9000 rpm for 10 min. The precipitate was washed three times with excess deionized water before being dried in an oven set at 50 °C for 12 h. The dried precipitate was then pulverized before using it for characterization, synthesis of photocatalyst composite, and photodegradation studies.

### 2.2.2. Synthesis of a photocatalyst composite

The photocatalyst composite was produced by doping LDH clay with AgBr using a photo-assisted technique adapted from Chen et al. [29]. The quantities of LDH, AgNO₃, and NaBr utilized in this study were determined based on the investigations carried out by Tabana and Tichapondwa [30]. LDH clay amounting to 1 g was added to 200 mL of deionized water and dispersed through ultrasonication for 45 min. Subsequently, 0.46 g of AgNO₃ dissolved in 5 mL of deionized water was added to the LDH suspension. After mixing for 2 h, 20 mL of a 2 M NaBr solution was added to the suspension and stirred in the dark to prevent photoionization of the produced AgBr [31]. Thereafter, 20 mL of methanol was added as a hole scavenger before subjecting the mixture to visible light irradiation. This was to reduce silver ions to metallic silver, preventing them from reacting with other species and producing unwanted by-products. Centrifugation was used to collect the precipitate, which was then washed three times with deionized water and once with methanol.

### 2.3. Catalyst characterization

The photocatalysts were characterized to establish their elemental composition, mineralogy, morphology, and Brunauer-Emmett-Teller (BET) surface area. X-ray powder diffraction (XRD) spectra were determined using a PANalytical X'Pert Pro powder diffractometer in θ-θ configuration fitted with an X'Celerator detector and variable divergence with Fe-filtered Co-Kα radiation (λ = 1.789 Å) fixed slits. Data was collected in the angular range of 5 to 90° 2θ with a step size of 0.008° 2θ and 13 s scan step time. The mineral phases present were confirmed using X'Pert Highscore plus software, which indexed the spectra against the ICSD database. A Zeiss Ultra Plus field emission scanning electron microscope (FEG-SEM) was used to capture the SEM/EDS images. SEM samples were prepared by distributing the samples on carbon tape stuck

to a microscopy stub; the samples were then sputter coated with carbon under argon gas. A Jeol-2100F Field Emission Electron Microscope was used for Transmission Electron Microscope (TEM) analysis. A few milligrams of the photocatalysts were placed in well-marked vials before adding 3 mL of ethanol. The suspensions were sonicated for 15 min to dissolve the photocatalysts. Small droplets of the dispersed samples were placed onto a TEM grid and allowed to dry in air. The dried grids were individually mounted onto a specimen holder for TEM analysis. The surface elemental compositions and electrochemical states of the photocatalysts were established through X-ray photoelectron spectroscopy (XPS) analysis. The analysis was conducted using a Thermo Fisher Scientific ESCALAB 250Xi coupled with a monochromatic Al Kα X-ray source (1486.7 eV) operated at 300 W. A Micrometrics Tristar 3000 BET analyzer was used to determine the BET surface area. All samples were degassed for 24 h at 150 °C under a $10^{-5}$ Torr vacuum before analysis.

### 2.4. Photocatalytic degradation experiments

The degradation tests were conducted in a closed compartment lined with a reflective material. The compartment contained 3 magnetic stirrers with the radiation sources placed directly above them. Reaction vessels with a nominal capacity of 250 mL were employed as reactors. 100 mL of predetermined concentrations of EFV or NVP solution were used in each experiment, and the amount of photocatalyst loaded varied based on the experimental design. EVF and NVP stock solutions of 100 mg/L were made by dissolving 1 mg of each pollutant in a 10 mL solution containing equal parts methanol and deionized water. The suspensions were sonicated for 30 min to dissolve all solids. The stock solutions were diluted with deionized water to create other desired concentrations. Before switching on the light source, pollutant-catalyst suspensions were allowed to mix and equilibrate in the dark for 30 min. The initial pH of the solutions was adjusted by adding 0.1 M HCl for acidic solutions and the required amount of 0.1 M NaOH solution for alkaline solutions. Aliquots were withdrawn at predetermined intervals, filtered, and analyzed using a Waters Alliance 2695 HPLC. This instrument was fitted with a UV–vis detector and an auto sampler. A Waters PAH C18 column was used for separation, while Empower Software was used to collect and analyse data. Elution was accomplished through a
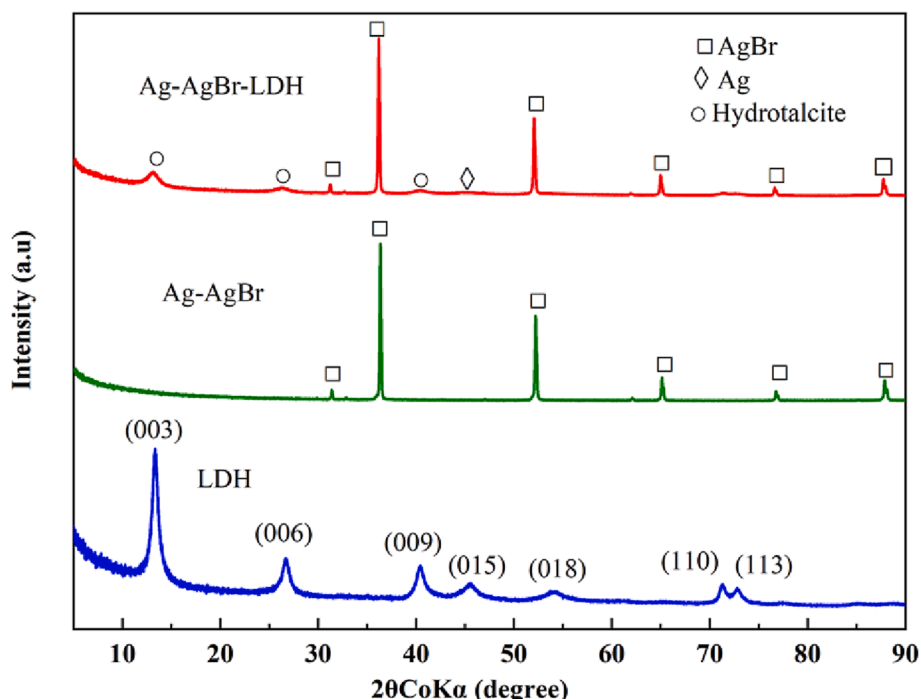


**Fig. 1.** (a) X-ray diffraction spectra of neat LDH, Ag-AgBr and Ag-AgBr-LDH composite catalysts.
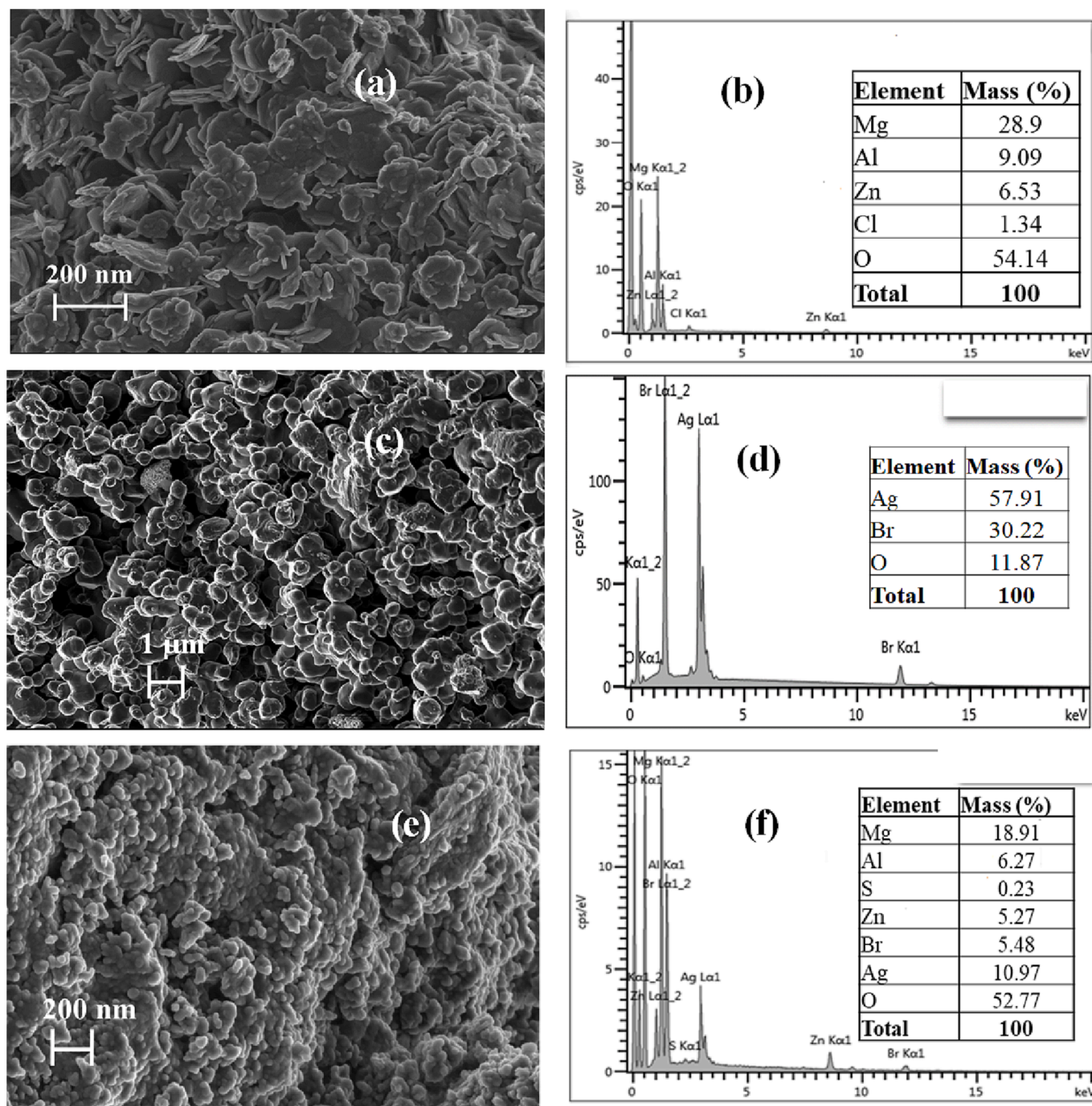
**Fig. 2.** SEM and SEM-EDS analysis of LDH (a) & (b), Ag-AgBr (c) & (d) and Ag-AgBr-LDH (e) & (f) photocatalysts.

gradient flow of a mobile phase composed of acetonitrile, methanol, and a pH 4.5 buffer solution. The mobile phase used to analyze the pollutants was separated into 2 distinct fractions. Mobile phase (1) contained acetonitrile, methanol, and a pH 4.5 buffer solution in the ratios of 60:15:25, whereas mobile phase (2) contained the same components in the proportions of 50:15:35. The two mobile phases were delivered using a gradient elution method as follows: 0 – 4 min with 100% mobile phase (1), 4.01 – 8 min with 100% mobile phase (2), and 8.01 – 12 min with 100% mobile phase (1).

The experimental plan was divided into two sections. In the first section, photodegradation tests were carried out using different photocatalysts, namely Ag-AgBr, LDH, and Ag-AgBr-LDH, to determine the most effective one. The tests were conducted under neutral pH condi-

tions, with an initial concentration of 10 mg/L, and a photocatalyst loading of 2 g/L. The photocatalyst that demonstrated the highest performance was subsequently used in the second section for parameter optimization tests. Design Expert software (version 13.0, Stat-Ease, Minneapolis, United States) was utilized to design a series of experiments and optimize the levels of the process parameters, A: photocatalyst loading (0.5 – 4 g/L), B: initial solution pH (5 – 12), and C: initial pollutant concentration (5 – 20 mg/L). A total of 22 experimental runs were simulated using an optimal design with four levels for each parameter. The three parameters were identified as independent variables, while degradation efficiency was chosen as the response output variable. The optimal values for the process variables were determined using a three-dimensional response surface modelling (RSM). Analysis
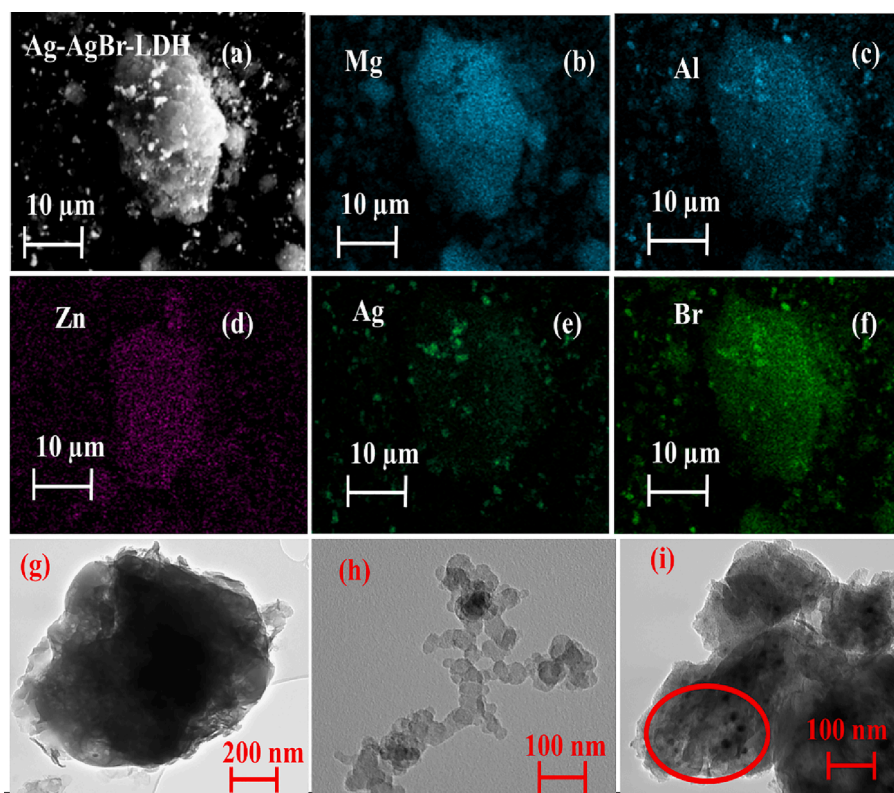
**Fig. 3.** HAADF-STEM image of Ag-AgBr-LDH (a), EDS mapping, Mg (b), Al (c), Zn (d), Ag (e) & Br (f). TEM images, LDH (g), Ag-AgBr (h) & Ag-AgBr-LDH (i)

of variance (ANOVA) was used to analyze the data, with p < 0.05 indicating a significant difference between the means. The experimental data were fitted to the quadratic equation shown in Equation (1) for statistical analysis. Equation (2) was used to determine the experimental response (photodegradation efficiency (%)).

$$Y = P_0 + \sum_{i=1} P_i x_i + \sum_{i=1}^{k} \sum_{j=1}^{k} P_{ij} x_i x_j \sum_{i=1}^{k} P_{ii} x_{ii} + \varepsilon \qquad (1)$$

$$Y = \left(1 - \frac{C_t}{C_0}\right) \times 100 \qquad (2)$$

Where Y represents the response; $P_0$ is the intercept; $P_i$, $P_{ij}$ and $P_{ii}$ are coefficients of the linear effect and double interactions; $x_i$ and $x_j$ are independent variables; $\varepsilon$ is error; $C_t$ and $C_0$ are pollutant concentration at time t and initial concentration in mg/L.

After optimizing the process parameters, kinetics studies were conducted at initial concentrations of 5, 10, and 20 mg/L. The primary radicals responsible for degradation were identified using scavenger tests. The photostability and reusability tests were conducted by recovering the used photocatalyst from the solution, washing it with deionized water, and drying it at 60 °C for 12 h before reusing it 3 times.

## 3. Results and discussion

### 3.1. Catalyst characterization

#### 3.1.1. Phase identification of photocatalysts

The XRD patterns of the neat, Ag-AgBr and doped LDH were determined through XRD analysis (Fig. 1). The characteristic peaks of the LDH clay were identified at the following angles: 13.2°, 26.6°, 40.2°, 45.1°, 54.8°, 72.1° and 73.2°. These peaks were assigned the following planes: (0 0 3), (0 0 6), (0 1 2), (0 1 5), (0 1 8), (1 1 0) and (1 1 3), respectively. These results confirmed the formation of LDH clay with carbonate ions ($CO_3^{2-}$) in the interlayer region [29]. The positions of the basal

planes, d-spacing, crystal parameters (c and a) and the crystallite size (L) for LDH and Ag-AgBr-LDH are shown in Table S1 in the supplementary data. The XRD patterns of the composite catalyst Ag-AgBr-LDH revealed the presence of both LDH and AgBr in the material. A feint peak in the composite at 2θ of 45° was designated to $Ag^0$ [32] (an XRD report of the Ag-AgBr-LDH spectra is shown in Fig. S1 in the supplementary data). This confirmed the success in synthesis of the desired photocatalyst and coexistence of $Ag^0$, AgBr and LDH in the composite.

#### 3.1.2. Scanning electron microscopy and transmission electron microscope analyses of photocatalysts

The morphologies of LDH clay, Ag-AgBr and Ag-AgBr-LDH photocatalysts are shown in Fig. 2. LDH clay was characterized by platelet-like structures that are synonymous with hydrotalcites (Fig. 2(a)). Ag-AgBr photocatalyst exhibits irregular spherical-like shapes, as demonstrated in Fig. 2 (c) [33]. The presence of minute particles in Fig. 2(c) could plausibly be attributed to the partial reduction of $Ag^+$ ions within the AgBr compound. Fig. 2(e) displays the morphology of the composite catalyst which shows the LDH platelet-like structures covered by near-spherical Ag-AgBr nanoparticles. The elemental compositions of the LDH clay, Ag-AgBr and Ag-AgBr-LDH photocatalysts were examined using energy dispersive X-ray spectroscopy (EDS) and the results are presented in Fig. 2(b), 2(d) and 2(f) respectively. The elemental analysis conducted on both LDH clay and the Ag-AgBr-LDH composite confirmed the presence of Mg, Zn, and Al in both materials. Additionally, the molar ratios of Ag to bromine Br were determined to be 1.43 and 1.48 in Ag-AgBr and Ag-AgBr-LDH composite photocatalyst, respectively. These ratios indicated an excess of Ag relative to Br, providing further evidence of the successful formation of $Ag^0$ in the photocatalyst composite.

Fig. 3 (a) – (f) depict the High-Angle Annular Dark-Field Scanning Transmission Electron Microscopy (HAADF-STEM) image and EDS elemental mapping images of the Ag-AgBr-LDH composite photocatalyst. The HAADF-STEM (Fig. 3(a)) image provides a representation of the composite photocatalyst, revealing the spatial distribution and
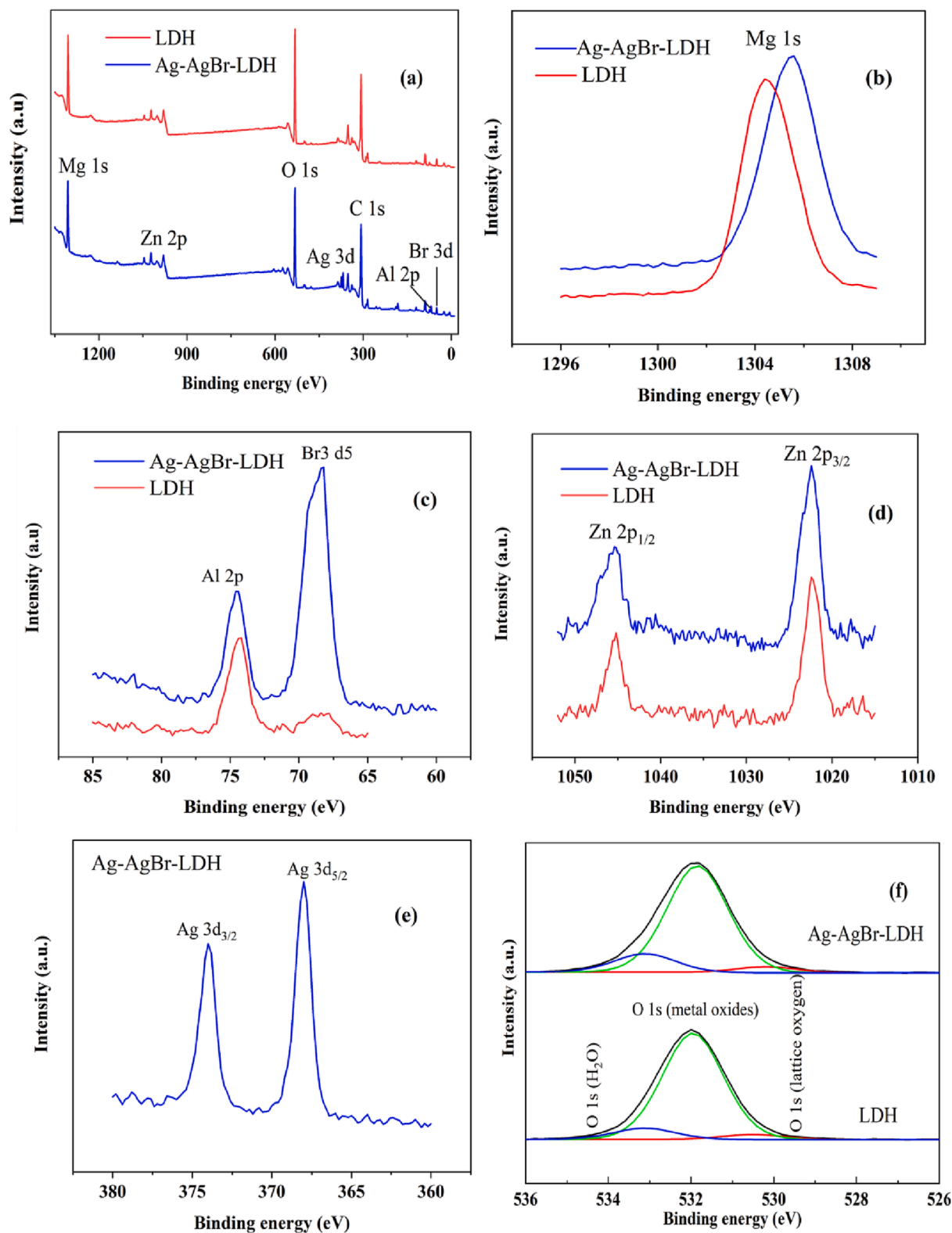
**Fig. 4.** XPS spectrum of LDH and Ag-AgBr-LDH photocatalysts (a) The survey spectrum peaks and the high resolution XPS spectra of (b) Mg 1S, (c)Br 3d5, (d) Zn 2p 3, (e) Ag 3d and (f) O 1 s.

arrangement of different elements. The elemental maps (Fig. 3(b) – (f)) indicate the presence and distribution of Mg, Al, Zn, Ag, and Br. Notably, the well-distributed elements in their respective regions confirm the successful loading of Ag-AgBr particles onto the LDH clay substrate. Fig. 3(g) – (i) show the results obtained from TEM analysis of LDH clay,

Ag-AgBr, and Ag-AgBr-LDH photocatalyst. The TEM image of LDH clay (Fig. 3(g)) exhibits a well-structured morphology, suggesting a high level of crystallinity in the material. This observation is consistent with the findings from XRD analysis, further supporting the crystalline nature of LDH clay. In Fig. 3(h), distinct near-spherical Ag-AgBr particles are
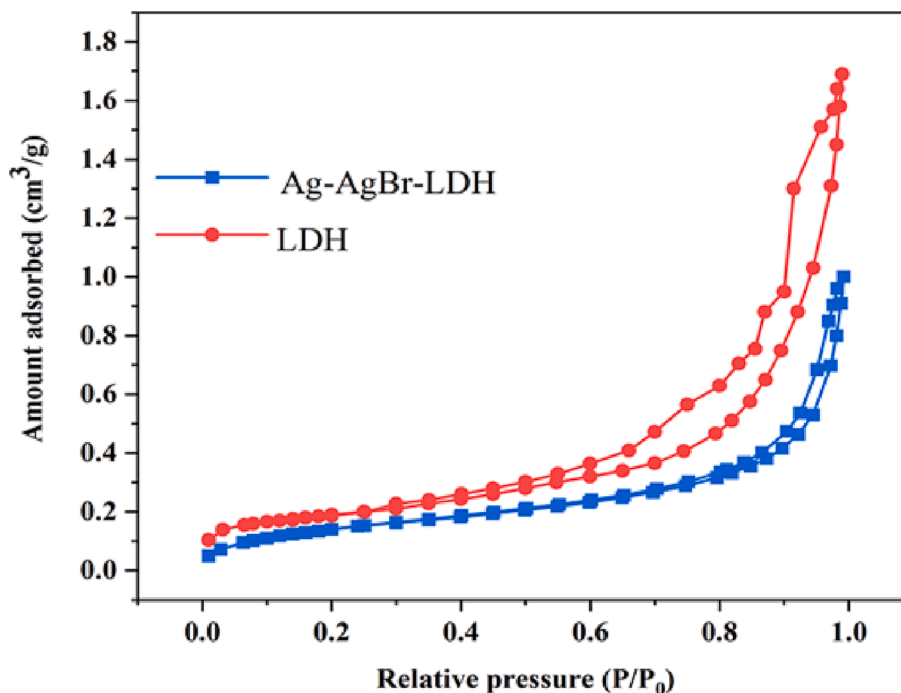
**Fig. 5.** Nitrogen adsorption–desorption isotherms of LDH and Ag-AgBr-LDH.

clearly visible. Notably, Fig. 3(i) highlights the encircled area where Ag-AgBr particles are observed in close proximity to the LDH clay substrate. These findings confirm the successful embedding of Ag-AgBr particles onto the LDH clay.

### 3.1.3. X-ray photoelectron spectroscopy analysis

The X-ray photoelectron spectroscopy (XPS) spectra for LDH and Ag-AgBr-LDH photocatalysts are shown in Fig. 4. The Mg 1 s spectra (Fig. 4 (b)) at the binding energies of 1304.4 and 1305.6 for LDH and Ag-AgBr-LDH photocatalyst respectively were attributed to the magnesium containing hydroxides [34]. The Al 2p spectra (Fig. 4(c)) at 74.6 eV displayed only one peak that showed the presence of aluminium containing hydroxides [35]. In Fig. 4(d), Zn enriched hydroxides are represented by the Zn $2p_{3/2}$ and Zn $2p_{1/2}$ peaks located at 1022.2 and 1045.4 eV respectively [34]. The Ag3d spectra (Fig. 4(e) displayed two individual peaks at 368 and 374 eV which were ascribed to Ag $3d_{5/2}$ and $3d_{3/2}$ of $Ag^0$ and $Ag^+$. The Ag 3d spectra in this study are similar to those reported by Liu *et. al.* [36], Wang *et. al.* [37] and Zhang *et. al.* [38], who stated that the peak at 368 eV was due to $Ag^0$ while $Ag^+$ was represented at 374 eV. These results are in agreement with XRD spectra for the composite catalyst which also revealed the presence of $Ag^0$. The peak at 68 eV in the Br 3d spectrum (Fig. 4(d)) was attributed to the crystal lattice of $Br^-$ in AgBr [39]. The O 1 s spectra showed 3 peaks at 532.2, 532 and 530 eV representing O in adsorbed water, metal hydroxides and lattice oxygen respectively [40].

### 3.1.4. Brunauer-Emmett-Teller (BET) surface area

Fig. 5 depicts the nitrogen gas adsorption and desorption isotherms of LDH and Ag-AgBr-LDH. The isotherm curves correspond to Type IV isotherms in accordance with IUPAC classification [41]. This showed that the photocatalysts had mesopores with a diameter range of 2–50 nm [42]. Doping the LDH with Ag-AgBr NPs resulted in decreased pore volume (0.075 $cm^3$/g to 0.022 $cm^3$/g) and specific surface area (28.5 $m^2$/g to 10.6 $m^2$/g) compared to neat LDH.
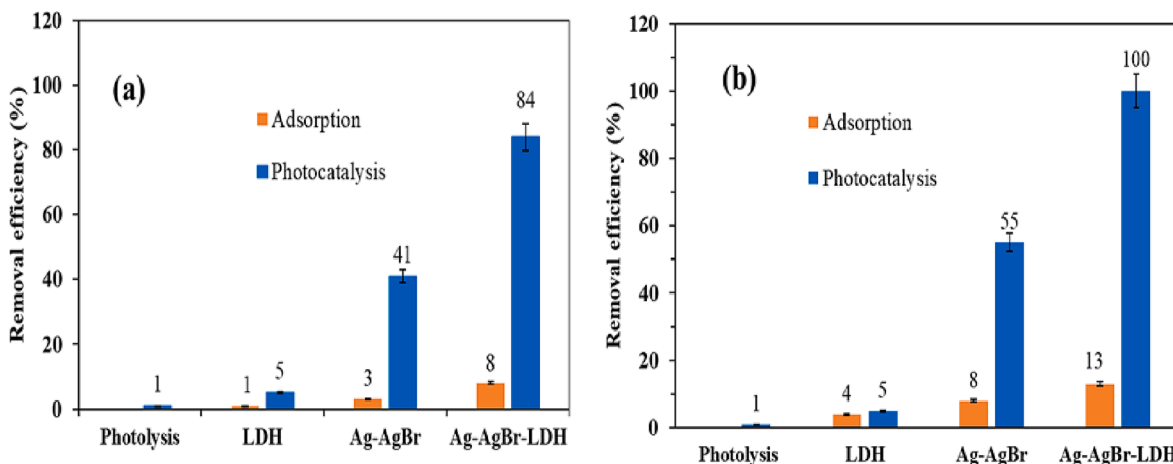


**Fig. 6.** Photodegradation efficiencies of ARVDs using various photocatalysts, (a) efavirenz and (b) nevirapine.

**Table 1**
Experimental runs and the corresponding degradation efficiencies for efavirenz and nevirapine.

| Run | A: Photocatalyst loading (g/L) | B: pH | C: Pollutant concentration (mg/L) | Efavirenz degradation efficiency (%) | Nevirapine degradation efficiency (%) |
|---|---|---|---|---|---|
| 1 | 0.5 | 5 | 15 | 16.2 | 18.9 |
| 2 | 0.5 | 9 | 10 | 44.7 | 49.5 |
| 3 | 2 | 9 | 5 | 40.2 | 43.2 |
| 4 | 4 | 5 | 5 | 18.6 | 20.2 |
| 5 | 4 | 5 | 5 | 22.8 | 18.7 |
| 6 | 2 | 7 | 15 | 42.3 | 46.3 |
| 7 | 4 | 12 | 20 | 68.6 | 73.6 |
| 8 | 4 | 12 | 20 | 32.9 | 27.9 |
| 9 | 0.5 | 5 | 5 | 74.3 | 71.4 |
| 10 | 2 | 5 | 10 | 42.4 | 37.3 |
| 11 | 4 | 5 | 20 | 29.9 | 32.9 |
| 12 | 2 | 12 | 15 | 42.5 | 45.7 |
| 13 | 4 | 12 | 5 | 34.6 | 27.6 |
| 14 | 4 | 5 | 20 | 35.8 | 33.7 |
| 15 | 0.5 | 9 | 20 | 24.8 | 19.3 |
| 16 | 4 | 12 | 5 | 38.6 | 42.7 |
| 17 | 0.5 | 5 | 5 | 45.8 | 41.7 |
| 18 | 4 | 7 | 10 | 24.9 | 18.3 |
| 19 | 2 | 5 | 20 | 27.7 | 33.3 |
| 20 | 4 | 9 | 15 | 12.5 | 6.9 |
| 21 | 1 | 12 | 20 | 75.4 | 72.9 |
| 22 | 0.5 | 12 | 5 | 75.4 | 72.9 |

**Table 2**
Analysis of variance for the quadratic model (efavirenz).

| Source | Sum of Squares | Degrees of freedom | Mean Square | F-value | p-value |
|---|---|---|---|---|---|
| **Model** | 5031.45 | 6 | 838.57 | 30.13 | < 0.0001 |
| A-Phtotocatalyst loading | 4159.04 | 1 | 4159.04 | 149.42 | < 0.0001 |
| B-pH | 60.86 | 1 | 60.86 | 2.19 | 0.0163 |
| C-pollutant concentration | 837.42 | 1 | 837.42 | 30.08 | 0.0001 |
| AC | 520.1 | 1 | 520.1 | 18.68 | 0.0008 |
| $A^2$ | 663.83 | 1 | 663.83 | 23.85 | 0.0003 |
| $C^2$ | 168.05 | 1 | 168.05 | 6.04 | 0.0288 |
| **Residual** | 361.86 | 13 | 27.84 | | |
| Lack of Fit | 207.33 | 8 | 25.92 | 0.8386 | 0.6081 |
| Pure Error | 154.52 | 5 | 30.9 | | |
| **Cor Total** | 5434.23 | 21 | | | |

**Table 3**
Analysis of variance for the quadratic model (nevirapine).

| Source | Sum of Squares | Degrees of freedom | Mean Square | F-value | P-value |
|---|---|---|---|---|---|
| **Model** | 4949.94 | 7 | 707.13 | 35.45 | < 0.0001 |
| A-Phtotocatalyst loading | 4174.68 | 1 | 4174.68 | 209.28 | < 0.0001 |
| B-pH | 95.76 | 1 | 95.76 | 4.8 | 0.0489 |
| C-pollutant concentration | 821.6 | 1 | 821.6 | 41.19 | < 0.0001 |
| AB | 52.44 | 1 | 52.44 | 2.63 | 0.0131 |
| AC | 535.21 | 1 | 535.21 | 26.83 | 0.0002 |
| $A^2$ | 707.42 | 1 | 707.42 | 35.46 | < 0.0001 |
| $C^2$ | 84.31 | 1 | 84.31 | 4.23 | 0.0622 |
| **Residual** | 239.37 | 12 | 19.95 | | |
| Lack of Fit | 195.17 | 7 | 27.88 | 3.15 | 0.1122 |
| Pure Error | 44.2 | 5 | 8.84 | | |
| **Cor Total** | 5200.01 | 21 | | | |

### 3.2. Photocatalytic degradation

#### 3.2.1. Degradation of ARVDs using various photocatalysts

Fig. 6 shows the removal efficiencies of EFV (Fig. 6(a)) and NVP (Fig. 6(b)) for the composite photocatalyst and its constituents under control conditions, adsorption, photolysis, and visible light irradiation. LDH clays are well-known for their ability to remove pollutants via a variety of mechanisms such as surface adsorption, intercalation [28,43], and adsolubilization [44]. Noting that the LDH clay in this study was neither calcined nor did its interlayer anions undergo modification, surface adsorption was most likely to occur. However, since the bonding forces involved in physical adsorption of pollutants onto LDH clay are weak [45], the adsorption efficiencies of neat LDH were limited to 5%. The Ag-AgBr photocatalyst could only degrade 41% of EFV and 55% of NVP under visible light irradiation, with adsorption efficiencies for both pollutants falling below 10%. However, the Ag-AgBr-LDH nano-composite photocatalyst demonstrated adsorption efficiencies of up to 13% and significantly improved photodegradation efficiencies of 84% and 100% for EFV and NVP, respectively. This enhancement can be attributed to surface plasmon resonance and/or z-scheme hetero-junction formation [23]. The $Ag^0$ nanoparticles in the photocatalyst can improve the photocatalyst's light-harvesting capacity via surface plasmon resonance and act as electron mediators in the formation of a Z-scheme heterojunction [23]. LDH and AgBr play essential roles as photo-induced electron and hole sinks, respectively. After determining that Ag-AgBr-LDH was the most effective photocatalyst, parameter optimization tests with this photocatalyst were performed.

#### 3.2.2. Statistical analysis of the ARVDs photodegradation process using ANOVA

Table 1 shows the results of the experimental design for the degradation efficiencies of two ARVDs. Tables 2 and 3 show the ANOVA results for EFV and NVP, respectively. The quadratic polynomial equations (Equations (3) and (4)) were derived using relative parameters to optimize the conditions for maximizing the degradation efficiencies of the ARVDs. ANOVA was utilized to assess the significance and adequacy of the quadratic models in describing the experimental data. The statistical significance of each variable and its effect on the response were determined using p-values and F-values at a 95% confidence level. Variables with p-values<0.05 were considered to be statistically significant. F-values of 30.13 for EFV and 35.45 for NVP indicated that the second-order polynomial models were highly significant. The probability that these F-values resulted from random noise was estimated to be 0.01%.

$$Y_E = 86.69 + 16.87A - 1.98B - 7.75C + 6.69AC - 14.50A^2 + 7.16C^2 \qquad (3)$$
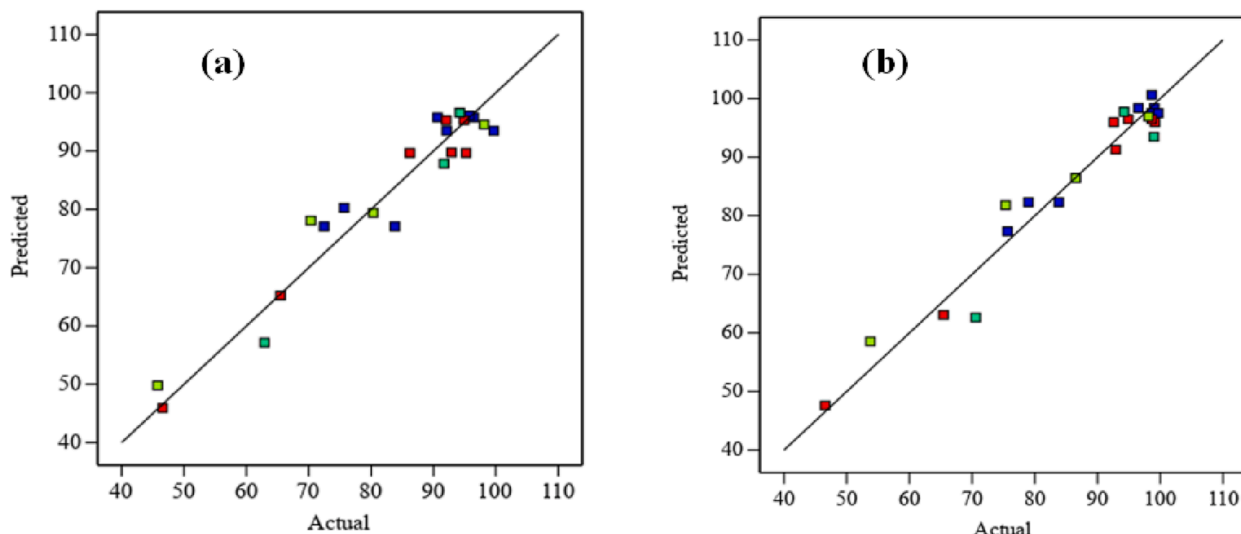
**Fig. 7.** Comparison between the predicted and actual responses (c) efavirenz and (d) nevirapine.
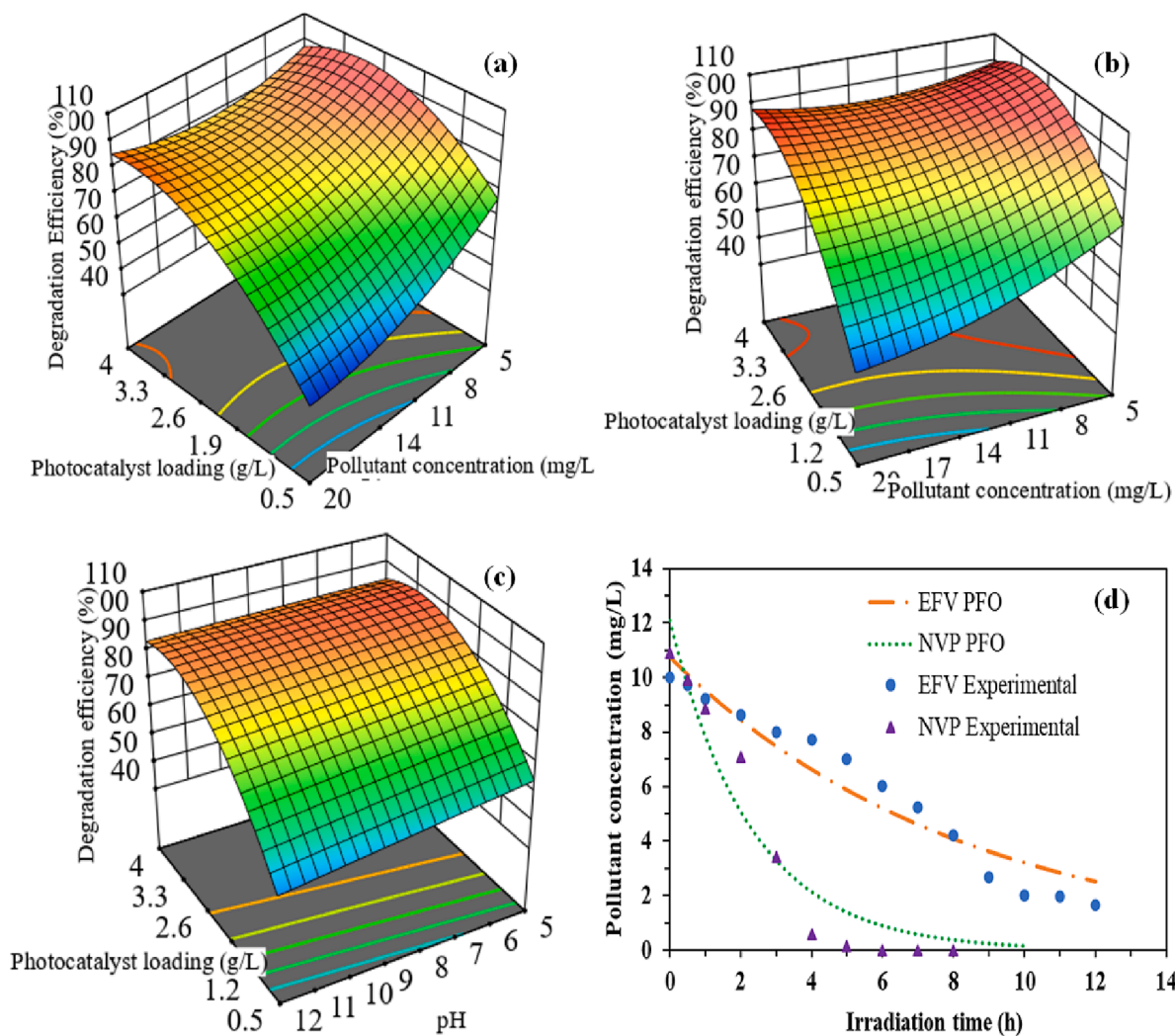


**Fig. 8.** (a) Response surface 3D plot for efavirenz, interactions between photocatalyst loading and pollutant concentration. Response surface 3D plot for nevirapine, (b) interactions between photocatalyst loading and pollutant concentration, (c) interaction between photocatalyst loading and initial pH of the solution. (d) PFO kinetics model fittings for efavirenz and nevirapine (10 mg/L).

**Table 4**
Photocatalytic degradation kinetics parameters.

| Pollutant | Parameter | Concentration (mg/L) | | |
|---|---|---|---|---|
| | | 5 | 10 | 20 |
| **Efavirenz** | k | 0.151 | 0.121 | 0.117 |
| | $R^2$ | 0.97 | 0.93 | 0.96 |
| **Nevirapine** | k | 0.585 | 0.433 | 0.322 |
| | $R^2$ | 0.985 | 0.941 | 0.965 |

$$Y_N = 91.48 + 17.07A - 2.62B - 7.70C + 2.28AB + 6.84AC - 15A^2 + 5.12C^2 \tag{4}$$

Where $Y_E$ and $Y_N$ represent the responses for EFV and NVP respectively.

Fig. 7 depict the actual and predicted response values for EFV (Fig. 7 (a)) and NVP (Fig. 7(b)), respectively. The close proximities of the actual and predicted experimental values to the straight lines in Fig. 7 indicate a good correlation between these values. Photocatalyst loading (A), initial pH of the solution (B), and pollutant concentration (C), second-order effects of photocatalyst loading ($A^2$) and pollutant concentration ($C^2$), and interactions between catalyst loading (A) and pollutant concentration (C) were statistically significant for EFV degradation. For NVP degradation, photocatalyst loading (A), initial pH of the solution (B), and pollutant concentration (C), second-order effects of photocatalyst loading ($A^2$) and pollutant concentration ($C^2$), and interactions between photocatalyst loading (A) and initial pH of the solution (B) and photocatalyst loading (A) and pollutant concentration (C) were statistically significant.

### 3.2.3. Optimization of process parameters using the response surface method

Fig. 8 (a) shows the degradation efficiency of EFV as a function of photocatalyst loading and pollutant concentration. For NVP, Fig. 8(b) and (c) show the degradation efficiency as functions of photocatalyst loading and pollutant concentration, and photocatalyst loading and pH respectively. The responses from Fig. 8 (a) and (b) are similar with the degradation efficiency being directly proportional to photocatalyst loading and inversely proportional to pollutant concentration. An increase in the amount of photocatalyst results in an increase in the active sites and a subsequent increase in degradation efficiency. However, when the pollutant concentration is increased, the ratio of active sites to pollutant molecules is reduced leading to decreased degradation efficiency. From Fig. 8 (c), photodegradation of NVP increased with an increase in photocatalyst loading irrespective of the change in pH. The effect of pH on photodegradation of NVP can be explained as follows: firstly, the point of zero charge for the photocatalyst was established to be 9.5 as shown in Fig. S2 in the supplementary data. This implied that the surface of the photocatalyst was positively charged at pH < 9.5 and negatively charged at pH greater than 9.5. Secondly NVP has a pKa of 2.8 [46] indicating that it is positively charged at pH < 2.8 and neutral at higher pH values. The operational pH of neutral fell within the region where the photocatalyst's surface was predicted to be positively charged while the NVP molecules were neutral. This enhanced the intermolecular interactions between the two components and enhanced the adsorption capacity, resulting in enhanced photocatalytic NVP degradation.

### 3.2.4. Photodegradation kinetics

The photocatalytic degradation kinetics of EFV and NVP were investigated by fitting a simple pseudo-first order (PFO) model (Equation (5)) to experimental data. Fig. 8(d) shows the fitted model for EFV and NVP at 10 mg/L (model fittings at 5 and 20 mg/L are shown in the supplementary data Fig. S3 and S4). The corresponding kinetics parameters are shown in Table 4. The results show that the degradation rate constants were inversely proportional to the initial concentration for the two pollutants, which can be attributed to numerous factors,

**Table 5**
Comparison of nevirapine photocatalytic degradation kinetics parameters.

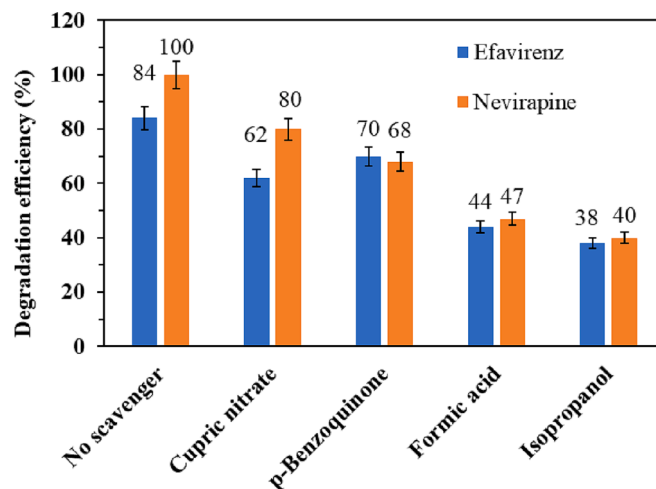| Photocatalyst | Initial concentration | Degradation efficiency (%) | Rate constant (1/h) | Reference |
|---|---|---|---|---|
| Ag-AgBr-LDH | 5 mg/L | 100 | 0.585 | this study |
| UV/TiO2/H2O2 | 40 µg/L | 89 | 2.2 | [52] |
| UV/H2O2 | 20 µg/L | 53 | 4.8 | [51] |
| UV/(FL-BP@Nb2O5) | 5 mg/L | 69 | 0.91 | [50] |



**Fig. 9.** Photodegradation efficiencies in the presence of various scavengers.

including competition for active sites between intermediate products and primary pollutant [47], a decrease in radical generation on the surface due to high pollutant concentrations [48], and light absorption by the pollutant, which leads to a reduction in active radical generation [49]. Furthermore, the photodegradation rate constants of NVP were compared to those reported in previous studies (Table 5), and it was determined that the rate constant at 5 mg/L (0.533/h) is comparable to that reported by Bhembe *et. al.* [50] (0.912/h) for a similar concentration. However, their overall degradation efficiency was lower compared to the total degradation in this study. Ngumba *et. al.* [51] and Ncube *et. al.* [52] reported higher degradation constants of 4.8 and 2.2 (1/h), respectively, but their pollutant concentrations were lower. It is also worth noting that previous studies were conducted under UV irradiation, whereas the current study used visible light irradiation. This demonstrates that Ag-AgBr-LDH is a viable photocatalyst for the degradation of EFV and NVP under visible light irradiation.

$$C = C_0 e^{-kt} \tag{5}$$

### 3.2.5. Scavenger tests and photodegradation mechanism

Fig. 9 shows degradation efficiencies of the two ARVDs in the presence of various radical scavengers. Isopropanol (IPA), p-benzoquinone (PBQ), copper (II) nitrate (CN) and formic acid (FA) were used as scavengers for hydroxyl radical ($^\bullet$OH), superoxide radical $^\bullet O_2^-$, electrons ($e^-$) and photo-induced holes ($h^+$), respectively. The degradation efficiency of both EFV and NVP decreased by 46 and 60% when IPA added. Significant reduction in degradation efficiency was also noted upon FA addition. These observations indicated that both $^\bullet$OH and $h^+$ played an important role in the degradation process. This accession was also reported by Ncube, Zvinowanda [52] and. Tafreshi *et. al.* [53]. The addition of PBQ and CN showed moderate reduction in degradation efficiencies of 14 and 22% for EFV, 32 and 22% for NVP. This implied that the superoxide radicals and the electrons were not the major drivers
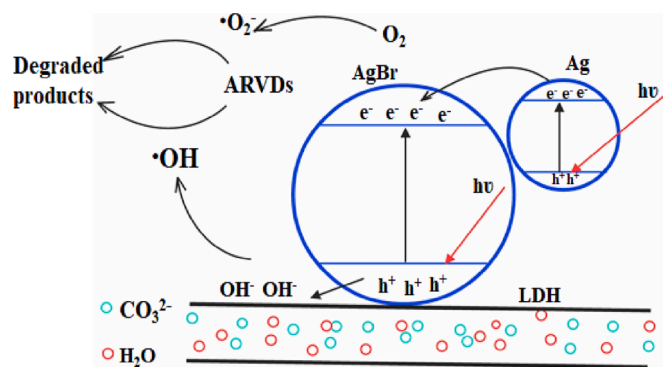
**Fig. 10.** Formation of major active species during visible light irradiation of photocatalyst.

of the photodegradation process.

The proposed mechanism for the photocatalytic degradation of ARVDs involves the generation of electron-hole pairs on the surface of silver nanoparticles through surface plasmon resonance (SPR) when exposed to light as shown in Fig. 10. The photo-excited silver nanoparticles then transfer electrons to the conduction band of AgBr, leading to the formation of $^{\bullet}O_2^-$ and other oxidants. The resulting silver nanoparticles can shift to a more positive potential, which allows them to either oxidize contaminants or capture electrons to revert back to non-charged Ag nanoparticles. The surface of LDH clays is covered with $OH^-$, which can accept the photo-induced holes from the valence band of AgBr to produce $^{\bullet}OH$. The binding of Ag-AgBr particles to LDH clay increases the probability of occurrence of this process. This is further supported by the scavenger tests, which demonstrated that when $^{\bullet}OH$ and $h^+$ were scavenged, the photodegradation efficiencies decreased substantially.

### 3.2.6. Photo-stability and reusability of the photocatalyst

The composite photocatalyst was recycled in a series of tests to evaluate its stability and reusability. Fig. 11 shows a gradual decrease in the degradation efficiency after the first two runs from 84% to 80% (EFV) and 100% to 95% (NVP). Thereafter, there were 24 and 21% decrease in efficiencies for EFV and NVP after Run 4. The decline in

photodegradation efficiencies was due to the inevitable deactivation of the photosensitive AgBr that is unstable under visible light irradiation [54,55]. This deactivation can cause aggregation of $Ag^0$ followed by a disfigured heterojunction structure. Ultimately the SPR property of silver nanoparticles become compromised giving rise to poor stability of the photocatalyst. Therefore, it can be postulated that the increased amounts of $Ag^0$ caused photo-corrosion of the photocatalyst which resulted in a decline in degradation efficiency.

### 4. Conclusion

A photocatalyst containing Ag-AgBr and LDH clay was successfully synthesized through photo-induced reduction method. This composite proved to be more effective in degrading the ARVDs (efavirenz and nevirapine) than Ag-AgBr and LDH clay separately. The response surface modelling showed the interaction between photocatalyst loading and initial concentration was significant for efavirenz while the interactions between pH and photocatalyst loading, and photocatalyst loading and initial concentration were significant for nevirapine. More than 80% and 100% of efavirenz and nevirapine were degraded over 12 and 8 h at neutral pH, under visible light irradiation. The hydroxy free radicals and photo-induced holes were established to be the active species responsible for degradation of ARVDs.

### CRediT authorship contribution statement

**Lehlogonolo Tabana:** Investigation, Funding acquisition, Formal analysis, Data curation, Conceptualization, Software, Writing – original draft, Writing – review & editing. **Davy-Rayn Booysens:** Investigation, Data curation, Writing – original draft, Formal analysis. **Shepherd Tichapondwa:** Conceptualization, Methodology, Validation, Formal analysis, Data curation, Visualization, Resources, Supervision, Project administration, Funding acquisition, Writing – review & editing.

### Declaration of Competing Interest

The authors declare that they have no known competing financial interests or personal relationships that could have appeared to influence the work reported in this paper.
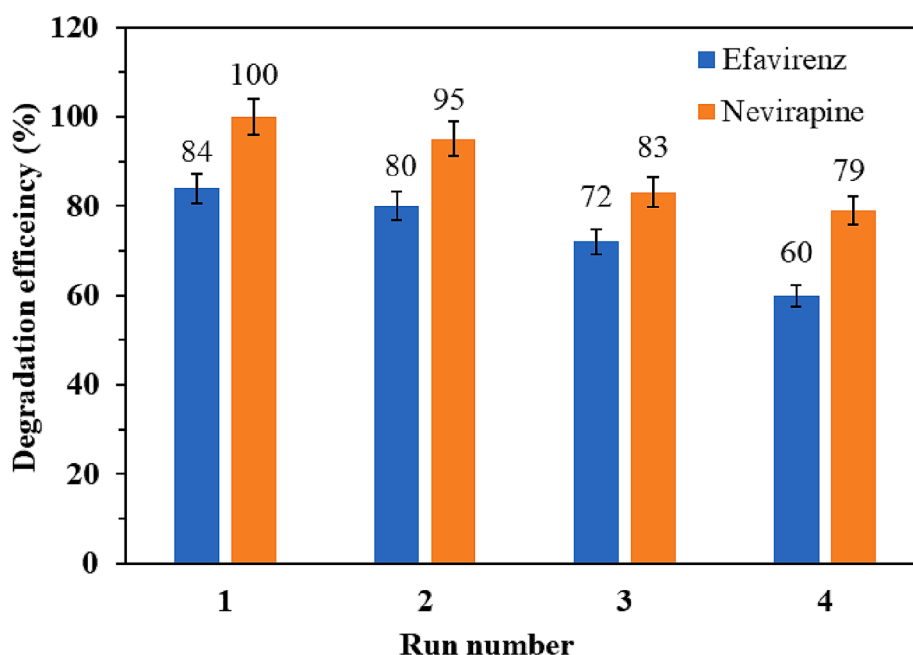


**Fig. 11.** Photostability and reusability of the photocatalyst.

## Data availability

Data will be made available on request.

## Acknowledgement

## Appendix A. Supplementary data

Supplementary data to this article can be found online at https://doi.org/10.1016/j.jphotochem.2023.114997.

## References

[1] A.O. Adeola, P.B. Forbes, Antiretroviral drugs in african surface waters: Prevalence, analysis, and potential remediation, Environ. Toxicol. Chem. 41 (2022) 247–262, https://doi.org/10.1002/etc.5127.

[2] S. Ncube, L.M. Madikizela, L. Chimuka, M.M. Nindi, Environmental fate and ecotoxicological effects of antiretrovirals: A current global status and future perspectives, Water Res. 145 (2018) 231–247, https://doi.org/10.1016/j.watres.2018.08.017.

[3] C. Schoeman, M. Dlamini, O. Okonkwo, The impact of a wastewater treatment works in southern Gauteng, South Africa on efavirenz and nevirapine discharges into the aquatic environment, Emerg. Contam. 3 (2017) 95–106, https://doi.org/10.1016/j.emcon.2017.09.001.

[4] T. aus der Beek, F.A. Weber, A. Bergmann, S. Hickmann, I. Ebert, A. Hein, A. Küster, Pharmaceuticals in the environment—global occurrences and perspectives, Environ. Toxicol. and Chem. 35 (2016) 823 – 835. https://doi.org/10.1002/etc.3339.

[5] C.M. Thorp, Pharmacology for the health care professions, John Wiley & Sons, Oxford, 2008.

[6] R. Cristofoletti, A. Nair, B. Abrahamsson, D. Groot, S. Kopp, P. Langguth, J.E. Polli, V.P. Shah, J.B. Dressman, Biowaiver monographs for immediate release solid oral dosage forms: Efavirenz, J. Pharm.Sci. 102 (2013) 318–329, https://doi.org/10.1002/jps.23380].

[7] Boehringer Ingelheim, Viramune® (nevirapine) Tablets/Viramune® (nevirapine) oral suspension, U.S. prescribing information. https://docs.boehringer-ingelheim.com/Prescribing%20Information/PIs/Viramune/Viramune.pdf, 2019 (accessed 14 March 2023).

[8] O.A. Abafe, J. Späth, J. Fick, S. Jansson, C. Buckley, A. Stark, B. Pietruschka, B.S. Martincigh, Lc-MS/MS determination of antiretroviral drugs in influents and effluents from wastewater treatment plants in KwaZulu-Natal, South Africa, Chemosphere 200 (2018) 660–670, https://doi.org/10.1016/j.chemosphere.2018.02.105.

[9] A.B. Zitha, S. Ncube, N. Mketo, H. Nyoni, L.M. Madikizela, Antiretroviral drugs in water: An African challenge with Kenya and South Africa as hotspots and plausible remediation strategies, Chem. Afr. 5 (2022) 1237–1253, https://doi.org/10.1007/s42250-022-00417-1.

[10] N. Mahaye, N. Musee, Effects of two antiretroviral drugs on the crustacean Daphnia magna in river water, Toxics 10 (2022) 423, https://doi.org/10.3390/toxics10080423.

[11] C.R. Souza, M. de Freitas Ribeiro, M. de Fátima Soares, S.F. dos Santos, C.A. de Jesus Pereira, M.P.G. Mol, M.R. Silveira, 2022. Environmental elimination estimate and literature review of ecotoxicological aspects of the main widely used antiretrovirals in Brazil. Res. Soc. Dev. 11, e368111032975. https://doi.org/10.33448/rsd-v11i10.32975.

[12] K. Jothivenkatachalam, A. Pandikumar, Photocatalytic functional materials for environmental remediation, first ed., John Wiley & Sons, New Jersey, 2019.

[13] S. Naseem, B. Gevers, R. Boldt, F.J.W. Labuschagné, A. Leuteritz, Comparison of transition metal (Fe Co, Ni, Cu, and Zn) containing tri-metal layered double hydroxides (LDHs) prepared by urea hydrolysis, RSC Adv. 9 (2019) 3030–3040, https://doi.org/10.1039/C8RA10165E.

[14] J.S. Valente, F. Tzompantzi, J. Prince, J.G. Cortez, R. Gomez, Adsorption and photocatalytic degradation of phenol and 2, 4 dichlorophenoxiacetic acid by Mg-Zn-Al layered double hydroxides, Appl Catal B 90 (2009) 330–338, https://doi.org/10.1016/j.apcatb.2009.03.019.

[15] S. Kim, P. Durand, E. André, C. Carteret, Enhanced photocatalytic ability of Cu, Co doped ZnAl based mixed metal oxides derived from layered double hydroxides, Colloids Surf A Physicochem Eng Asp 524 (2017) 43–52.

[16] B.L. Diffey, Sources and measurement of ultraviolet radiation, Methods 28 (2002) 4–13, https://doi.org/10.1016/S1046-2023(02)00204-9.

[17] A. Sherryna, M. Tahir, Recent developments in layered double hydroxide structures with their role in promoting photocatalytic hydrogen production: A comprehensive review, Int. J. Energy Res. 46 (2022) 2093–2140, https://doi.org/10.1002/er.7335.

[18] S.F. Ng, M.Y.L. Lau, W.J. Ong, Engineering layered double hydroxide–based photocatalysts toward artificial photosynthesis: State-of-the-art progress and prospects, Sol. Rrl. 5 (2021) 2000535, https://doi.org/10.1002/solr.202000535.

[19] L. Liu, S. Li, Y. An, X. Sun, H. Wu, J. Li, X. Chen, H. Li, Hybridization of nanodiamond and CuFe-LDH as heterogeneous photoactivator for visible-light driven photo-fenton reaction: Photocatalytic activity and mechanism, Catal. 9 (2019) 118, https://doi.org/10.3390/catal9020118.

[20] A. Akbarzadeh, Y. Khazani, S.S. Khaloo, M. Ghalkhani, Highly effectual photocatalytic degradation of tartrazine by using Ag nanoparticles decorated on Zn-Cu-Cr layered double hydroxide@ 2d graphitic carbon nitride ($C_3N_5$), Environ. Sci. Pollut. Res. 30 (2023) 12903–12915, https://doi.org/10.1007/s11356-022-23001-z.

[21] B. Luo, R. Song, D. Jing, ZnCr LDH nanosheets modified graphitic carbon nitride for enhanced photocatalytic hydrogen production, Int. J. Hydrogen Energy 42 (2017) 23427–23436, https://doi.org/10.1016/j.ijhydene.2017.03.001.

[22] M. Wu, J. Wu, J. Zhang, H. Chen, J. Zhou, G. Qian, Z. Xu, Z. Du, Q. Rao, A review on fabricating heterostructures from layered double hydroxides for enhanced photocatalytic activities, Catal, Sci. Technol. 8 (2018) 1207–1228, https://doi.org/10.1039/C7CY02314F.

[23] J. Zheng, X. Tang, C. Fan, Y. Deng, X. Li, Q.i. Yang, D. Wang, A. Duan, J. Luo, Z. Chen, B. Zhang, Facile synthesis of Ag@ AgCl/ZnAl-LDH sesame balls nanocomposites with enhanced photocatalytic performance for the degradation of neonicotinoid pesticides, Chem. Eng. J. 446 (2022), 136485, https://doi.org/10.1016/j.cej.2022.136485.

[24] M.M. Khan, D. Pradhan, Y. Sohn, Nanocomposites for visible light-induced photocatalysis, Springer, Switzerland, 2017.

[25] B. Weng, M.Y. Qi, C. Han, Z.R. Tang, Y.J. Xu, Photocorrosion inhibition of semiconductor-based photocatalysts: Basic principle, current development, and future perspective, ACS Catal. 9 (2019) 4642–4687, https://doi.org/10.1021/acscatal.9b00313.

[26] K. Huang, C. Li, Y. Zheng, L. Wang, W. Wang, X. Meng, Recent advances on silver-based photocatalysis: Photocorrosion inhibition, visible-light responsivity enhancement, and charges separation acceleration, Sep. Purif. Technol. 283 (2022), 120194, https://doi.org/10.1016/j.seppur.2021.120194.

[27] S.K. Sharma, P.K. Kushwaha, V.K. Srivastava, S.D. Bhatt, R.V. Jasra, Effect of hydrothermal conditions on structural and textural properties of synthetic hydrotalcites of varying Mg/Al ratio, Ind. Eng. Chem. Res. 46 (2007) 4856–4865, https://doi.org/10.1021/ie061438w.

[28] L. Tabana, S. Tichapondwa, F. Labuschagne, E. Chirwa, Adsorption of phenol from wastewater using calcined magnesium-zinc-aluminium layered double hydroxide clay, Sustain. 12 (2020) 4273, https://doi.org/10.3390/su12104273.

[29] C. Chen, H. Zeng, J. Xiong, S. Xu, D. An, Z-scheme AgBr@ Ag/coal layered double hydroxide heterojunction for superior photocatalytic Cr (vi) reduction under visible light, Appl. Clay Sci. 192 (2020) 105627, https://doi.org/10.1016/j.clay.2020.105627.

[30] L.S. Tabana, S.M. Tichapondwa, Photocatalytic degradation of phenol using visible light activated Ag-AgBr-hydrotalcite composite, Chem. Eng. Trans. 99 (2023) 259–264, https://doi.org/10.3303/CET2399044.

[31] S. Svanstrom, T.J. Jacobsson, G. Boschloo, E.M. Johansson, H. Rensmo, U.B. Cappel, Degradation mechanism of silver metal deposited on lead halide perovskites, ACS Appl. Mater. Interfaces 12 (2020) 7212–7221, https://doi.org/10.1021/acsami.9b20315.

[32] S. Feng, T. Chen, Z. Liu, J. Shi, X. Yue, Y. Li, Z-scheme CdS/CQDs/g-$C_3N_4$ composites with visible-near-infrared light response for efficient photocatalytic organic pollutant degradation, Sci. Total Environ. 704 (2020), 135404, https://doi.org/10.1016/j.scitotenv.2019.135404.

[33] M.M. Moja, E. Chirwa, S.M. Tichapondwa, Visible light activated photocatalytic degradation of 2, 4-dichlorophenol using silver halide photocatalysts, Chem. Eng. Trans. 86 (2021) 1411–1416, https://doi.org/10.3303/CET2186236.

[34] Y.X. Zhu, G.L. Song, P.P. Wu, J.F. Huang, D.J. Zheng, A protective superhydrophobic Mg-Zn-Al LDH film on surface-alloyed magnesium, J. Alloy Compd. 855 (2021), 157550. https://doi.org/10.1016.j.jallcom.2020.157550.

[35] H. Wang, Y. Zhu, Z. Hu, X. Zhang, S. Wu, R. Wang, Y. Zhu, A novel electrodeposition route for fabrication of the superhydrophobic surface with unique self-cleaning, mechanical abrasion and corrosion resistance properties, Chem. Eng. J. 303 (2016) 37–47, https://doi.org/10.1016/j.cej.2016.05.133.

[36] C. Liu, W. Sun, Y. Zhuo, C. Liu, Y. Chu, PVP-assisted synthesis and visible light catalytic property of Ag/AgBr/$TiO_2$ ternary nanostructures, J. Alloy. Compd. 581 (2013) 115–120, https://doi.org/10.1016/j.jallcom.2013.07.019.

[37] P. Wang, B. Huang, X. Qin, X. Zhang, Y. Dai, M.H. Whangbo, Ag/AgBr/$WO_3$·$H_2O$: Visible-light photocatalyst for bacteria destruction, Inorg. Chem. 48 (2009) 10697–10702, https://doi.org/10.1021/ic9014652.

[38] S. Zhang, I. Khan, X. Qin, K. Qi, Y. Liu, S. Bai, Construction of 1d Ag-AgBr/AlOOH plasmonic photocatalyst for degradation of tetracycline hydrochloride, Front. Chem. 8 (2020) 117, https://doi.org/10.3389/fchem.2020.0011.

[39] T. Parvizi, J.B. Parsa, R. Farnood, Synergetic photocatalytic fuel cell and CuFe layered doubled hydroxide as photoactivator of persulfate for dramatically electricity generation of organic pollutants degradation, Appl. Catal. B (2022), 121894, https://doi.org/10.1016/j.apcatb.2022.121894.

[40] S. Nayak, K. Parida, Dynamics of charge-transfer behavior in a plasmon-induced quasi-type-II p-n/n-n dual heterojunction in Ag@ $Ag_3PO_4$/g-$C_3N_4$/NiFe LDH nanocomposites for photocatalytic Cr (vi) reduction and phenol oxidation, ACS Omega 3 (2018) 7324–7343, https://doi.org/10.1021/acsomega.8b00847.

[41] M. Muttakin, S. Mitra, K. Thu, K. Ito, B.B. Saha, Theoretical framework to evaluate minimum desorption temperature for iupac classified adsorption isotherms, Int. J. Heat Mass Transf. 122 (2018) 795–805, https://doi.org/10.1016/j.ijheatmasstransfer.2018.01.107.

[42] P. Tun, K. Wang, H. Naing, J. Wang, G. Zhang, Facile preparation of visible-light-responsive kaolin-supported Ag@ AgBr composites and their enhanced

photocatalytic properties, Appl. Clay Sci. 175 (2019) 76–85, https://doi.org/10.1016/j.clay.2019.04.003.

[43] X. Lei, M. Jin, G.R. Williams, Layered double hydroxides in the remediation and prevention of water pollution, Energy Environ, Focus 3 (2014) 4–22, https://doi.org/10.1166/eef.2014.1086.

[44] X. Ruan, S. Huang, H. Chen, G. Qian, Sorption of aqueous organic contaminants onto dodecyl sulfate intercalated magnesium iron layered double hydroxide, Appl. Clay Sci. 72 (2013) 96–103, https://doi.org/10.1016/j.clay.2013.01.001.

[45] J. Cornejo, R. Celis, I. Pavlovic, M. Ulibarri, Interactions of pesticides with clays and layered double hydroxides: A review, Clay Miner. 43 (2008) 155–175, https://doi.org/10.1180/claymin.2008.043.2.01.

[46] S. Kim, J. Chen, T. Cheng, A. Gindulyte, J. He, S. He, Q. Li, B.A. Shoemaker, P. A. Thiessen, B.o. Yu, L. Zaslavsky, J. Zhang, E.E. Bolton, New data content and improved web interfaces, Nucleic Acids Res. 49 (D1) (2021) D1388–D1395.

[47] V. Hequet, C. Raillard, O. Debono, F. Thévenet, N. Locoge, L. Le Coq, Photocatalytic oxidation of vocs at ppb level using a closed-loop reactor: The mixture effect, Appl Catal B 226 (2018) 473–486, https://doi.org/10.1016/j.apcatb.2017.12.041.

[48] M.R.D. Khaki, M.S. Shafeeyan, A.A.A. Raman, W.M.A.W. Daud, Application of doped photocatalysts for organic pollutant degradation: A review, J. Environ. Manage. 198 (2017) 78–94, https://doi.org/10.1016/j.jenvman.2017.04.099.

[49] S. Ahmed, F.S.A. Khan, N.M. Mubarak, M. Khalid, Y.H. Tan, S.A. Mazari, R.R. Karri, E.C. Abdullah, Emerging pollutants and their removal using visible-light responsive photocatalysis–a comprehensive review, J. Environ. Chem. Eng. 9 (2021) 106643, https://doi.org/10.1016/j.jece.2021.106643.

[50] Y.A. Bhembe, L.P. Lukhele, L. Hlekelele, S.S. Ray, A. Sharma, D.V.N. Vo, L. N. Dlamini, Photocatalytic degradation of nevirapine with a heterostructure of few-layer black phosphorus coupled with niobium (v) oxide nanoflowers (FL-BP@ $Nb_2O_5$), Chemosphere 261 (2020), 128159, https://doi.org/10.1016/j.chemosphere.2020.128159.

[51] E. Ngumba, A. Gachanja, T. Tuhkanen, Occurrence of selected antibiotics and antiretroviral drugs in nairobi river basin, Kenya, Sci. Total Environ. 539 (2016) 206–213, https://doi.org/10.1016/j.scitotenv.2015.08.139.

[52] P. Ncube, C. Zvinowanda, M. Belaid, F. Ntuli, Heterogeneous photocatalytic degradation of nevirapine in wastewater using the UV/$TiO_2$/$H_2O_2$ process, Environ. Processes 10 (2022) 1–24, https://doi.org/10.21203/rs.3.rs-1823748/v1.

[53] N. Tafreshi, S. Sharifnia, S. Moradi Dehaghi, Photocatalytic treatment of a multicomponent petrochemical wastewater by floatable ZnO/oak charcoal composite: Optimization of operating parameters, J. Environ. Chem. Eng. 7 (5) (2019), 103397, https://doi.org/10.1016/j.jece.2019.103397.

[54] C. Xue, X. Yan, S. Ding, G. Yang, Monodisperse Ag-AgBr nanocrystals anchored on one-dimensional $TiO_2$ nanotubes with efficient plasmon-assisted photocatalytic performance, RSC Adv. 6 (2016) 68653–68662, https://doi.org/10.1039/C6RA13269C.

[55] Y. Yang, W. Guo, Y. Guo, Y. Zhao, X. Yuan, Y. Guo, Fabrication of z-scheme plasmonic photocatalyst Ag@ AgBr/g-$C_3N_4$ with enhanced visible-light photocatalytic activity, J. Hazard. Mater. 271 (2014) 150–159, https://doi.org/10.1016/j.jhazmat.2014.02.023.